



# The Properties of the Galactic Hot Gaseous Halo from X-Ray Emission

Yunyang Li<sup>1</sup> and Joel Bregman<sup>2</sup><sup>1</sup> Peking University, Beijing 100871, China; [liyongyang@pku.edu.cn](mailto:liyongyang@pku.edu.cn)<sup>2</sup> University of Michigan, 1085 S. University Avenue, Ann Arbor, MI 40109, USA

Received 2017 June 15; revised 2017 September 28; accepted 2017 October 9; published 2017 November 7

## Abstract

The extended hot X-ray emitting gaseous halo of the Milky Way has an optical depth  $\sim 1$  for the dominant emission lines of O VII and O VIII, which are used to infer the halo properties. To improve on halo gas properties, we treat optical depth effects with a Monte Carlo radiative transfer model, which leads to slightly steeper density profiles ( $\beta \approx 0.5$ ) than if optical depths effects were ignored. For the preferred model where the halo is rotating on cylinders at  $180 \text{ km s}^{-1}$ , independent fits to both lines lead to identical results, where the core radius is  $2.5 \text{ kpc}$  and the turbulent component of the Doppler- $b$  parameter is  $100\text{--}120 \text{ km s}^{-1}$ ; the turbulent pressure is 20% of the thermal pressure. The fit is improved when emission from a disk is included, with a radial scale length of  $3 \text{ kpc}$  (assumed) and a fitted vertical scale height of approximately  $1.3 \text{ kpc}$ . The disk component is a minor mass constituent and has low optical depth, except at low latitudes. The gaseous mass is  $3\text{--}4 \times 10^{10} M_{\odot}$  within  $250 \text{ kpc}$ , similar to our previous determinations and significantly lower than the mass of the missing baryons, which is  $1.7 \times 10^{11} M_{\odot}$ .

**Key words:** Galaxy: halo – X-rays: diffuse background

## 1. Introduction

Galaxy formation through spherical accretion naturally produces an accretion shock with gas near the virial temperature  $T_{\text{vir}}$  (White & Frenk 1991). This picture is modified by radiative losses and non-spherical accretion, leading to cooled gas, but still with a hot halo present. Simulations (e.g., Cen & Ostriker 2006; De Lucia et al. 2006; Kim et al. 2009; Tang et al. 2009; Crain et al. 2010; Joung et al. 2012) show that hot halos are prominent in more massive galaxies ( $M_{\text{halo}} \geq 10^{11.4} M_{\odot}$ , Kereš et al. 2005), where the cooling time is longer. The mass of the hot gaseous halo is modified significantly by feedback, especially in the region where  $t_{\text{cool}} < t_{\text{Hubble}}$ . The hot halo may be important from the census of metals and baryons. Compared to cosmological observation (Hinshaw et al. 2013), most of the baryons and metals are missing from galaxies (see Bregman 2007, for a review). It is suggested that a significant fraction of the missing baryons and metals lies in an extended hot halo, out to or beyond  $R_{\text{vir}}$  (Fukugita et al. 1998; Nicastro et al. 2005; Williams et al. 2005, 2006, 2007; Fukugita & Peebles 2006; Sommer-Larsen 2006).

We detect extended halos around some external galaxies, both in field early-type galaxies (Forman et al. 1985; O’Sullivan et al. 2001; Mulchaey & Jeltama 2010) and in spiral galaxies (Bregman & Houck 1997; Tüllmann et al. 2006; Li et al. 2008; Anderson & Bregman 2011; Dai et al. 2012; Bogdán et al. 2013a, 2013b; Walker et al. 2015). However, the structure and content of early-type galaxies are likely to be affected by the merger history and the interaction with the intergroup/intracluster medium in which most large ellipticals reside (Mulchaey & Jeltama 2010). The X-ray luminosities for isolated early-type galaxies and late-type galaxies fall below the detection limit at radii beyond  $\sim 0.1 R_{\text{vir}}$  (Anderson et al. 2016). In contrast, observing from the interior provides us an unparalleled opportunity to study the hot halo around the Milky Way.

At the Milky Way’s virial temperature ( $\approx 2 \times 10^6 \text{ K}$ ), the O VII and O VIII lines act as ideal tracers for the hot gas because

their emissivities are most sensitive at this temperature (Sutherland & Dopita 1993). By probing the O VII absorption against more than  $\sim 30$  AGNs and X-ray binaries, the local hot medium is studied in absorption lines (Nicastro et al. 2002; McKernan et al. 2004; Williams et al. 2005, 2006, 2007; Yao & Wang 2005; Hagihara et al. 2010; Gupta et al. 2012; Yao et al. 2012; Miller & Bregman 2013; Fang & Jiang 2014; Hodges-Kluck et al. 2016; Nicastro et al. 2016) and is suggested to be associated with the Galaxy (i.e., rather than with the intergroup hot gas; Fang et al. 2006; Bregman & Lloyd-Davies 2007). The studies of diffuse Milky Way emission from empty fields has started with the *ROSAT* sky survey (Snowden et al. 1995, 1997) and continues with more data from subsequent observatories (McCammon et al. 2002; Yao et al. 2009; Gupta et al. 2012; Henley & Shelton 2013). Combined with absorption data, the constraints on the halo property are obtained, which are accordant with external galaxy observation.

The optical depth effects of the hot gas are important in line analyses, and the studies are carried out progressively for absorption lines. Miller & Bregman (2013) use O VII absorption toward 29 targets from the *XMM-Newton* Reflection Grating Spectrometer (RGS) archival data, and they include the curve-of-growth analysis to correct the column density for optical depth effects. Assuming that the turbulence of the halo is  $b = 150 \text{ km s}^{-1}$ , the authors obtain  $n_0 = 0.46^{+0.74}_{-0.35} \text{ cm}^{-3}$ ,  $r_c = 0.35^{+0.29}_{-0.27} \text{ kpc}$ , and  $\beta = 0.71^{+0.13}_{-0.14}$ , which is slightly different from the values obtained via an optically thin analysis and lead to a lower baryon mass estimate ( $1.2 \times 10^{10} M_{\odot}$ , compared to  $2.4 \times 10^{10} M_{\odot}$  in the optically thin case). In the study of a more comprehensive set of absorption lines, Fang et al. (2015) fit the Doppler- $b$  parameters, which are consistent with  $98.0 \pm 19.4 \text{ km s}^{-1}$ . Studies probing the column density and Doppler- $b$  parameter are also carried out through the absorption line ratios approach. Gupta et al. (2012) measure the equivalent width (EW) ratio between O VII  $K\alpha$  and  $K\beta$  lines and place a constraint on the Doppler  $b$  for each sight line. Their results indicate that most (six out of eight of their sample)

O VII  $K\alpha$  lines are indeed saturated with the Doppler- $b$  =  $95.0 \pm 17.1$  km s<sup>-1</sup>. A similar analysis has also been performed recently by Nicastro et al. (2016) for low and high galactic latitude sight lines, and they find the mean Doppler- $b$  values to be 125 km s<sup>-1</sup> and 95 km s<sup>-1</sup>, respectively. Nevalainen et al. (2017) perform an elaborate analysis on the local absorption spectra of blazar PKS 2155-304 to study the ionization of the hot halo as well as lower temperature plasmas. Their results for the O VII lines indicate a Doppler  $b$  of about 80 km s<sup>-1</sup>.

The emission properties of the halo are studied in Miller & Bregman (2015) (hereafter, MB15), in which the authors use the emission map of O VII and O VIII from Henley & Shelton (2012) and fit the observation to the halo model. They calculate the line intensities with an optically thin model, and correct the optical depth effects by a mean scattering term (i.e., a single-scattered scenario). By separately fitting the data with and without the optical depth effects, they reach similar but different results, based on which they constrain the halo model well and claim that the optical depth effects are partially considered. However, for their best-fit result of O VIII,  $n_0 r_c^{3\beta} = 1.5$  cm<sup>-3</sup> kpc<sup>3 $\beta$</sup> , where  $\beta = 0.54$  and assuming a Doppler width of 150 km s<sup>-1</sup>, the optical depths toward the Galactic center and anticenter at the line centroid (18.96 Å) are 2.45 and 0.45, respectively, indicating that most photons are scattered more than once along the path. Moreover, if the hot gas is less turbulent, e.g., the entire contribution for the Doppler width is from the thermal motion of the plasma at  $\approx 50$  km s<sup>-1</sup>, the optical depth will be greater than 1 at all directions. If the halo is truly turbulent, then a mean scattering term will not be valid. In either case, the optical depth effect should be included in any determination of the gas density distribution. The main purpose of this work is to incorporate a Monte Carlo radiative transfer (MCRT) simulation to reproduce the emission map and compare it with observations. In this way, we are able to constrain all model parameters to better precision. Moreover, we add other components to the hot gas model, such as the rotation of the halo and a disk-like component; these have been discussed in the literature (Yao et al. 2009; Hodges-Kluck et al. 2016; Nicastro et al. 2016).

The paper is structured as follows. In Section 2 we describe all model assumptions including the density profile and rotation profile of the hot gas halo. In Section 3 we explain the data reduction and introduce the simulation method. We present the results from the simulation and the improved constraints on the density profile in Section 4 and discuss them in Section 5.

## 2. Model

The analyses of the hot gaseous halo rest on the model assumptions. Here we explain all premises we make based on previous observations, which include the temperature, density, rotation profile, and metallicity model.

### 2.1. Galactic X-Ray Emission

In this work, we study the hot gas component of the Milky Way by extracting its information from a soft X-ray emission observation. However, the data are comprised of several constituents beyond the hot gaseous halo. Two local contributors of the soft X-ray background (SXRb) are the solar wind charge exchange process (SWCX) and the Local Bubble (LB). SWCX is X-ray emission that occurs when highly

ionized metals from the solar wind (O<sup>7+</sup>, O<sup>8+</sup> in our case) capture electrons from the neutral gas they interact with, either within the Earth's magnetosheath (Robertson & Cravens 2003) or in the heliosphere (Lallement 2004). For the former mechanism, it is dependent on the solar wind activity and therefore temporal variations on timescales of hours to days, while the latter varies more on direction than time. The method we used to account for the SWCX is discussed in Section 3.1.1. We have also known for decades the existence of a low-density cavity, which is an old superbubble in which the Sun resides (Cox & Reynolds 1987; Snowden et al. 1997). This LB is highly ionized at a temperature  $\sim 10^6$  K (Snowden et al. 1990), which makes it a contributor to the SXRb. However, the structure of the LB is still unclear. Evidence supports either a volume-filled bubble (Snowden et al. 1990; Smith et al. 2007) or a wall of gas (Welsh & Shelton 2009) at the edges of the bubble. In this work we adopt the constant-density volume-filled model used in MB15, and the details are discussed in Section 3.1.4.

### 2.2. Temperature

Owing to the sensitivity of the ion fraction of O VII and O VIII in the  $10^{6-7}$  K temperature range (Sutherland & Dopita 1993), the temperature estimates of the hot gas in the Milky Way reach good agreement at about  $\log T = 6.2-6.3$ , despite different measurements and model assumptions (McKernan et al. 2004; Yao & Wang 2005; Williams et al. 2007; Yao et al. 2009; Hagihara et al. 2010; Gupta et al. 2012). The best probe of the temperature structure comes from Henley & Shelton (2013), and it supports an isothermal temperature model. The authors use a subset (110 sight lines) of emission lines in Henley & Shelton (2012) to minimize contamination from the SWCX, process the data in a similar way to Henley & Shelton (2012), and fit the spectra with thermal plasma models for the hot gas halo. This work concludes a median temperature at  $2.22 \times 10^6$  K with an interquartile range of  $0.63 \times 10^6$  K, while the emission measure and intrinsic 0.5–2.0 keV flux varies by over an order of magnitude. Here we choose an intermediate value of  $2 \times 10^6$  K.

Theoretical emissivities of O VII and O VIII are obtained from AtomDB version 2.0.2 (Foster et al. 2012), which assumes an APEC thermal plasma in collisional ionization equilibrium (CIE, Smith et al. 2001, which is also assumed throughout our model), and solar abundance (Anders & Grevesse 1989), which is  $N_O/N_H = 8.5 \times 10^{-4}$ , whereas we adopt  $N_O/N_H = 5.5 \times 10^{-4}$  (Holweger 2001). Therefore we correct the emissivity obtained from AtomDB by a factor of  $5.5/8.5 = 0.65$ . At  $2 \times 10^6$  K, the emissivities in units of  $10^{-15}$  photons cm<sup>3</sup> s<sup>-1</sup> are  $\epsilon_{O\text{ VII}} = 3.09, 0.546, 2.395, 0.373$  for the r, i, f, and He $\beta$  lines and  $\epsilon_{O\text{ VIII}} = 1.45$ .

Since *XMM-Newton* EPIC-MOS is unable to resolve the O VII triplet as well as O VIII resonance and O VII He $\beta$ , we simulate the photons of the triplet to fit the O VII data and the photons from the other two channels to fit the O VIII data, although there are no optical depth effects for the O VII forbidden line and intercombination line because of their small oscillator strengths.

### 2.3. Density Profile

The density profile of the hot gaseous halo can be derived from the Navarro–Frenk–White model assuming an isothermal

temperature profile, and it can be well approximated by the King profile (or  $\beta$ -model, Mo et al. 2010),

$$n(r) = n_0 \left( 1 + \left( \frac{r}{r_c} \right)^2 \right)^{-3\beta/2}. \quad (1)$$

Given its success in describing early-type (Forman et al. 1985) and late-type galaxies (Dai et al. 2012) as well as our Milky Way (Miller & Bregman 2015; Nicastro et al. 2016), our simulation will mainly focus on this model. However, based on the absorption of X-ray binaries (Yao & Wang 2005) and the spectral analysis of diffuse gas along the LMC X-3 sight line (Yao et al. 2009), an exponential disk structure with a height scale of about  $1 \sim 3$  kpc has been suggested. A model combining the halo and a thin disk ( $<1$  kpc) is also favored by a joint study of low galactic and high galactic absorption lines (Nicastro et al. 2016). We begin by exploring the spherical  $\beta$ -model on the all-sky emission and consider the disk structure as a modification to the gas density.

This model is applied in MB15, and they obtain a set of best-fit parameters  $n_0 r_c^{3\beta} = 0.79 \pm 0.10 \times 10^{-2} \text{ cm}^{-3} \text{ kpc}^{3\beta}$ , and  $\beta = 0.45 \pm 0.03$  for O VII and  $n_0 r_c^{3\beta} = 1.50 \pm 0.24 \times 10^{-2} \text{ cm}^{-3} \text{ kpc}^{3\beta}$  and  $\beta = 0.54 \pm 0.03$  for O VIII. They only consider a power-law approximation  $n(r) = n_0 r_c^{3\beta} r^{-3\beta}$  without fitting the core radius because of the lack of sight lines toward the Galactic center. To compare with the previous work, we adopt the complete three-parameter density model and determine each simultaneously.

#### 2.4. Rotation

The hot halo is rotating in the same direction as the Galactic disk, based on observations of X-ray absorption lines against bright AGN continua, projected around the sky (Hodges-Kluck et al. 2016 obtained constraints on the radial velocity of  $v_r = -15 \pm 20 \text{ km s}^{-1}$  and on the azimuthal velocity of  $v_\phi = 183 \pm 41 \text{ km s}^{-1}$ ). In this work, the azimuthal velocity is fixed at  $v_\phi = 180 \text{ km s}^{-1}$  beyond 1 kpc and linearly drops to 0 within 1 kpc, while the inflow velocity is neglected.

The rotation of the hot gas halo influences X-ray emission lines in two ways: (1) the rotation of the halo shifts the line centroid, but this effect is irrelevant in our simulation as the spectra are not resolved, and (2) the line profiles are broadened and become non-Gaussian at lower latitude and directions away from the Galactic (anti-) center. The broadening effect can be described by an effective Doppler- $b$  parameter, defined as  $b = \sqrt{2}\sigma^2$ . A rotationally broadened profile reduces the net optical depth along the line of sight, and this effect can therefore be characterized in the radiative transfer simulation.

Miller et al. (2016) calculated absorption lines for different rotation models of the hot Galactic halo. Here, we present in Figure 1 the counterpart of these discussions for emission lines. In Figure 1, we assume the Doppler width  $b = 100 \text{ km s}^{-1}$ , and the result shows that the rotation effect is greatest at roughly midway between the Galactic center and the anticenter and decreases at higher latitudes.

#### 2.5. Other Parameters

Observations of the hot extended halos of external galaxies suggest a subsolar abundance (e.g., Anderson et al. 2016). Cosmological simulations (Toft et al. 2002; Cen & Ostriker

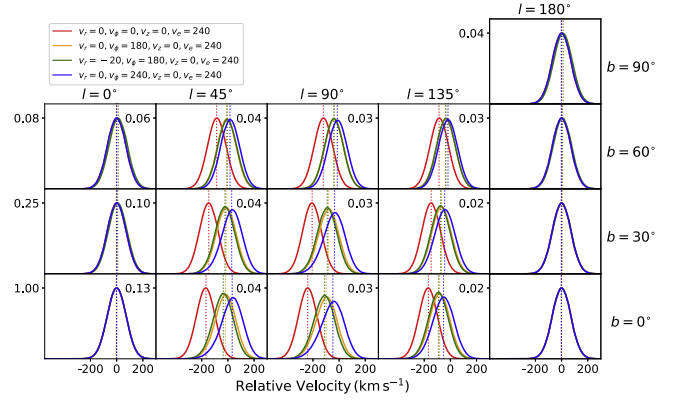


**Figure 1.** Numerical prediction for X-ray emission spectra across the sky. The rotation models are the same as those in Miller et al. (2016) and are color-coded in the same way as described in the legend, where  $v_r$ ,  $v_\phi$ ,  $v_z$  are the radial, azimuthal, and axial velocity of the halo in units of  $\text{km s}^{-1}$  and  $v_e$  is the speed of the Earth. The red curve stands for the stationary case. The additional orange curve is the model used in the simulation. The parameters are  $\beta = 0.5$ ,  $r_c = 2.5 \text{ kpc}$ , and  $b = 100 \text{ km s}^{-1}$ . The vertical axes are rescaled so that the peak intensity is 1 at  $l = b = 0^\circ$ .

2006), observations on external spirals (Rasmussen et al. 2009; Anderson et al. 2016), and high-velocity clouds (Gibson et al. 2000; van Woerden & Wakker 2004; Fox et al. 2005) agree on a metallicity of  $0.3 Z_\odot$ . We adopt this value since it has successfully been used to interpret data in Gupta et al. (2012), Miller & Bregman (2013, 2015), and Nicastro et al. (2016).

We adopt a solar distance  $d_\odot = 8.5 \text{ kpc}$  from the Galactic center (Ghez et al. 2008), along with the commonly accepted values  $R_{\text{vir}} = 250 \text{ kpc}$  and  $M_{\text{vir}} = 1.5 \times 10^{12} M_\odot$  for the virial radius and the virial mass.

### 3. Method

#### 3.1. Data Reduction

The data used here are almost identical to those in MB15, which are based on the catalog of *XMM-Newton* data produced by Henley & Shelton (2010, 2012). We therefore only briefly summarize the data reduction process as these former works contain detailed descriptions. In the following two subsections, we review the data selection and emission line measure analysis conducted in Henley & Shelton (2010, 2012). We also describe the additional filtering process MB15 use in Section 3.1.3. In Section 3.1.4 we describe the correction method applied to alleviate the effects from non-halo sources.

##### 3.1.1. Data Selection

The original data were taken from the catalog of *XMM-Newton* prior to August 2010, containing 5698 observations with MOS exposures, and they were processed with *XMM-Newton* Science Analysis System (SAS) version 11.0.1 (including the *XMM-Newton* Extended Source Analysis Software *XMM-ESAS*). Observing time affected by soft-proton flaring were removed, which is distinguished by the count rate of the 2.5–12.0 keV light curve at that interval, which differs from the mean value (fitted by a Gaussian) by more than  $1.5\sigma$ . Any observation with good observing time shorter than 5 ks or that does not have at least one MOS1 exposure and one MOS2 exposure was also discarded. Consequently, 2611 of the



original 5698 observations remained after this screening procedure.

The authors conducted a source removal procedure using the data from the *XMM-Newton* Serendipitous Source Catalog. Any point source within the field of view with flux in 0.5–2.0 keV band  $F_X^{0.5-2.0} \geq 5 \times 10^{-14} \text{ erg cm}^{-2} \text{ s}^{-1}$  was excised by a circle of radius  $50''$ , which encloses  $\approx 90\%$  of the source flux. In addition, bright sources not adequately removed by automatic processes and CCDs in anomalous states were excluded through visual inspection.

To reduce the contamination by SWCX, the authors used OMNIWeb, whose data are from satellites measuring the solar wind in situ (mainly the *Advanced Composition Explorer* and *Wind*), and excluded the time when the SWCX is prominent (indicated by solar wind proton flux exceeding  $2 \times 10^8 \text{ cm}^{-2} \text{ s}^{-1}$ ). This screening reduced the useful exposure times of some observations below the 5 ks threshold described above, which reduced the usable sight lines to 1435.

### 3.1.2. Emission Line Measure

Prior to extracting the emission line measurements, the authors subtracted the SXRb, including the SWCX, the Galactic and extra-galactic emission, the quiescent particle background and the residual soft-proton contamination, from the full field of view. The measurements were conducted with XSPEC version 12.7.0. For each observation, the authors fitted the data in 0.4–10.0 keV band with a multicomponent spectral model including two delta functions for the O VII and O VIII  $K_\alpha$  emission with the centroid for O VII left as a free parameter; the energy of O VIII is fixed at 0.6536 keV (from APEC; Smith et al. 2001). This method measured all oxygen line emission including that from the (residual) SWCX, LB emission, and attenuated halo emission. The Galactic and extra-galactic emission were modeled with an absorbed APEC thermal plasma model and an absorbed power-law (EPL) model with a photon index of 1.46, respectively. The authors also used a power law to model the residual contamination from the soft protons, although part of this effect was reduced through the cleaning method introduced above. The APEC and EPL component were attenuated using the XSPEC absorption model (Balucinska-Church & McCammon 1992; Yan et al. 1998) with H I column data from the LAB H I survey (Kalberla et al. 2005).

Henley & Shelton (2012) measured the statistical error and considered the uncertainties contributed from APEC and EPL fitting and combined the two in quadrature. To quantitatively account for the soft-proton contamination, the authors calculated the total flux in 2–5 keV,  $F_{\text{total}}^{2-5}$ , and its EPL component,  $F_{\text{exgal}}^{2-5}$ . The ratio of these two values was treated as a threshold, and any observation with the ratio below 2.7 was discarded. The final screening ruled out the soft-proton-contaminated observations and reduced the number of usable data from 1435 to 1003.

### 3.1.3. Further Screening

MB15 applied further screening methods to obtain the most reliable set of observations. They removed observations close to possible X-ray sources, including bright X-ray sources (ROSAT-BSC), galaxies (PGC 2003), galaxy clusters (MCXC), and quasars (ROSAT-RLQ; RQQ).

Some Galactic X-ray structures are also contaminations that should be avoided when characterizing the extended hot halo, such as supernovae and superbubbles. The large Galactic absorption correction at low latitudes can be rather uncertain because there is no all-sky  $\text{H}_2$  map. Therefore, MB15 excluded the observations with Galactic latitude  $l \leq 10^\circ$ . The Fermi Bubble (FB, Su et al. 2010) at the center of the Galaxy also exhibits strong X-ray emission, thus the observations with  $|l| \leq 22^\circ$  and  $|b| \leq 55^\circ$  were excluded. The region of the Fermi Bubbles is treated separately in Miller & Bregman (2016). Finally, they removed a cluster of data near the Large Magellanic Cloud and the Small Magellanic Cloud.

After all filtering processes, MB15 had 649 sight lines and conducted analyses to obtain best fits for the halo density profile. However, when they compared their best-fit model with O VIII data, they found that one observation (*XMM-Newton* ObsID 0200730201,  $(l, b) = 327^\circ 59', +68^\circ 92'$ ) was  $9\sigma$  above the model prediction ( $I_{\text{obs}} = 8.69 \text{ L.U.}$  compared to  $I_{\text{mod}} = 1.18 \text{ L.U.}$ , L.U. is the line unit:  $\text{photons cm}^{-2} \text{ s}^{-1}$ ), and the goodness-of-fit can be significantly improved from  $\chi_{645}^2 = 1.21$  to  $\chi_{644}^2 = 1.08$  when this observation is excluded. This excess of emission might due to the supernovae located within the north polar spur and should not be considered in our hot gas halo model. Although MB15 only exclude it for the O VIII analysis and used all 649 sight lines for O VII, we use only 648 observations for the O VII and O VIII lines.

### 3.1.4. Residual Corrections

The major Galactic components that must be corrected for when studying the hot halo include the emission from the FB and LB, the extinction effect of the disk, and the SWCX process. The effect of the FB has been eliminated by avoiding the sight lines through the bubbles, and the effect of the disk is partially alleviated in the same way. Regarding the Galactic absorption, considerable extinction can occur on individual sight lines, although sight lines from the disk (i.e.,  $|b| < 10^\circ$ ) are excluded. The LB with a temperature slightly below that of the halo also contributes to the emission line. Consequently, the observed intensities can be decomposed as

$$I_{\text{obs}} = I_{\text{halo}} e^{-\tau(N_{\text{H1}})} + I_{\text{LB}}. \quad (2)$$

The H I column and extinction rates at different lines of sight are obtained from HEASARC,<sup>3</sup> whose data are based on H I surveys (Dickey & Lockman 1990; Kalberla et al. 2005). Considerations for the LB are not as straightforward, and the contribution in the optically thin case is

$$I_{\text{LB}} = \frac{\epsilon_{\text{LB}}}{4\pi} \int_0^L n^2 ds. \quad (3)$$

However, the geometry of the LB is still unclear. We adopt the model in MB15, where they use a constant-density, volume-filled LB model with a uniform temperature and the boundary of the LB in every direction varies in the range 100–300 pc (Lallement et al. 2003). Therefore, the emissions from the LB become a linear function of its path length,

$$I_{\text{LB}} = \frac{\epsilon_{\text{LB}}}{4\pi} n^2 L. \quad (4)$$

<sup>3</sup> <https://heasarc.gsfc.nasa.gov>

The path length of each sight line is inferred from 1003 Na I absorption line EW measurements in Lallement et al. (2003). MB15 leave the constant of the LB density as a free parameter in the fitting process. Here, we use their best-fit values  $n = 4.0 \times 10^{-3} \text{ cm}^{-3}$  for O VII and  $n = 0.7 \times 10^{-3} \text{ cm}^{-3}$  for O VIII. We also use the same temperature assumption, i.e., that the LB is at  $\log T(K) = 6.1$ , which is lower than the halo temperature by a factor of 2.

### 3.2. Modeling Optical Depth Effects

MB15 fit a power-law density model to the emission data, but they did not determine the core radius independently from the normalized density parameter due to the lack of observations near the Galactic center. Their correction for the optical depth effect is limited to a simplification of the radiative transfer function—a single-scattering model. However, as is shown later, multi-scattering processes contribute a non-negligible part and affect the surface brightness distribution across the sky. In this section, we explain the principles of the radiative transfer code and how parameter choices affect our comparison with data.

#### 3.2.1. Monte Carlo Radiative Transfer

The essence of the simulation is to reproduce the radiative transfer process in the halo. The simulation focuses mainly on the propagation, not on the mechanisms of emission and absorption, therefore these physical processes are treated statistically in the context of photons. The emission is through collisional excitation of the CIE gas. Photons are emitted randomly in angle and subject to a radial distribution proportional to the squared density profile of the halo,

$$p(r) = Cr^2 n^2(r), \quad (5)$$

where  $C$  is a normalization. This distribution can be sampled, for any set of parameters, through an acceptance-rejection Monte Carlo method (Flury 1990).

The history of a photon is determined by the radiative transfer process, which is given by

$$\frac{d I_\nu}{d s} = -\kappa_\nu I_\nu, \quad (6)$$

where  $I_\nu$  is the specific intensity at a given frequency and  $\kappa_\nu$  is the extinction coefficient. The emission and scattering term do not appear because we are tracking every single photon rather than doing a field analysis.

In terms of discrete photons, the specific intensity can be written as (Whitney 2011)

$$I_\nu = \frac{h\nu N_{\nu,\Omega}}{\mu \Delta\mu \Delta\phi \Delta\nu \Delta A}, \quad (7)$$

where  $h\nu$  is the energy of the photon;  $\mu = \cos \theta$  is the cosine of the latitudinal angle, and the solid angle  $d\Omega = \mu d\mu d\phi$ ;  $A$  is the cross area. Consequently, the solution to the above equation is, in terms of photon number in a certain parameter range,

$$N_{\nu,\Omega}(\tau_{\nu,\Omega}) = N_0 e^{-\tau_{\nu,\Omega}}, \quad (8)$$

where  $d\tau_{\nu,\Omega} = \kappa_\nu d s(\Omega)$  is the optical depth. This solution can be understood in two equivalent ways. First, a group of photons runs synchronously, but the survival number of photons after each step (spatial or temporal) obeys an exponential

distribution dictated by the optical depth. Alternatively, a photon is stopped at a certain distance (absorbed or scattered), but this path length, in terms of optical depth, varies from one photon to another and is subject to the exponential distribution. In simulations, the latter interpretation is more computationally efficient and is adopted in this work.

At the beginning of the streaming of every photon, a random number subjected to the exponential distribution with an expectation of unity is sampled, which is interpreted as the optical depth of the free path of this photon. To determine the termination of the photon, the optical length is converted into geometric distance and fulfilled step by step. The smaller the step the photon takes, the better the accuracy of the terminal position. Here we chose a typical step at 0.3 kpc and adaptively scaled by a factor  $(r/r_c)^{3\beta}$  if the photon is far from the center, where the plasma is very diffuse. The conversion from optical depth into geometric length is calculated through

$$d\tau_\nu = \frac{\pi e^2}{m_e c} n_X f \phi(\nu) d s, \quad (9)$$

where the first term is the constant  $0.02654 \text{ cm}^2 \text{ s}^{-1}$ ,  $n_X$  the number density of absorbers, and  $f$  the oscillator strength.  $\phi(\nu)$  is the normalized line shape related to the Doppler parameter  $b$  by

$$\phi(\nu) = \frac{1}{\sqrt{\pi} \nu_D} e^{-\left(\frac{\nu-\nu_0}{\nu_D}\right)^2} \quad \nu_D = \frac{b}{c} \nu_0, \quad (10)$$

where  $\nu_0$  is the laboratory frequency and  $c$  is the speed of light.

For resonance lines, the photons are not destroyed but are absorbed and reemitted. The reemission is isotropic relative to the absorber and at a different frequency, based on the local Gaussian line shape. For a 0.5 keV X-ray photon, the Compton-scattering cross section is insignificant relative to the absorption cross section. Therefore there is no practical difference between scattering and absorption.

The simulation begins with a photon created somewhere inside the halo according to the density profile of Equation (1). The photon propagates repeatedly according to Equation (8) unless it is detected by the “telescope” or escapes the boundary of the halo. The total number of photons created and the number of photons detected gives the intensity as a function of angle, which is compared to the data. When the photons are collected, the geometric symmetry can be exploited to promote efficiency. For the stationary model (nonrotating gaseous halo), the system is spherically symmetric. Therefore every photon that reaches the sphere 8.5 kpc from the Galactic center (distance of the Sun from the Galactic center) is indistinguishable from each other and can be collected directly. The simulation effectively obtains the flux by counting the number of the photons reaching the solar sphere, and the flux should be divided by the projection term to obtain the specific intensity ( $\mu = \cos \theta$  in Equation (7)). In this case, where the detection surface is a sphere, the projection angle  $\theta$  is the angle between the sight line and the Galactic center).

In the case of a rotating halo, the cylindrical symmetry makes the simulation much more computationally intensive. The “telescope” is a ring that lies on the solar circle. Consequently, the projection onto the plane introduces a factor  $\cos \theta = \sin b$ , where  $b$  is the Galactic latitude.

### 3.3. Data Fitting

We compare the data of the 648 sight lines with our MCRT simulation. For a given set of simulation parameters ( $\Theta$ ), the fitness is described by  $\chi^2$ , defined as

$$\chi^2(\Theta) = \sum_{i=1}^{648} \frac{(I_i - s_i(\Theta))^2}{\sigma_i^2}, \quad (11)$$

where  $I_i$  and  $\sigma_i$  are the corrected intensity and error of the data;  $s_i$  is the intensity given by the simulation at the same location. The connotation of “same location” is different for the stationary and the rotating model.

For the stationary model, we contract the coordinates of the observation into its angle toward the Galactic center  $\theta$  and multiply them by the factor  $\cos \theta$  as the conversion from specific intensities into fluxes, and  $2\pi \sin \theta$  as the integral over the degenerate azimuthal angle. The collected photons are binned by 100 equal-width bins along the  $\theta$ -axis, and smoothed by a polynomial function to estimate their 1D distribution. The  $s_i$  values are chosen at the same  $\theta$  location as the smoothed histogram.

For the corotating model, we make 2D bins for both the 648 sight lines and the simulated emission map. Because of the mirror symmetry with respect to the  $b = 0$  plane,  $s_i$  is calculated by the weighted mean density of the photons within the bin of the  $i_{\text{th}}$  data sight line and the 8 bins around it and the mirror images of these 9 bins.

The parameters of interest are the three profile parameters,  $n_0$ ,  $\beta$ ,  $r_c$ , and the Doppler factor  $b$ . For the oxygen ions at  $T = 2.0 \times 10^6$  K, the thermal motion contributes  $b_{\text{th}} = 50 \text{ km s}^{-1}$  to the Doppler width. Here we are only interested in the nonthermal part of the Doppler width, therefore we sample  $b_{\text{turb}}$  and convert it into  $b_{\text{tot}} = \sqrt{b_{\text{turb}}^2 + b_{\text{th}}^2}$  in the simulation. To find the best combination of these parameters that is most consistent with the data, we adopt the Monte Carlo Markov chain (MCMC) method using the Python package *emcee* (Foreman-Mackey et al. 2013) to explore the parameter space. At each MCMC step, a set of parameters is chosen and the corresponding simulated data are generated through the MCRT, and the log-likelihood  $-0.5\chi^2$  is calculated to evaluate the goodness of the set of parameters.

## 4. Results

In this section we summarize the results from the MCRT-MCMC fitting. Similar to the method in MB15, we fit the two sets of ion lines separately because the O VII lines have a higher mean S/N (4.9), while that of O VIII is lower (1.3).

### 4.1. Stationary Model Parameter Estimation

For the stationary model, we use  $10^5$  photons in each MCMC step to obtain a simulated emission map with high S/N, and in turn, a relatively robust parameter estimation. The results for stationary model fitting are plotted in the upper panel of Figure 2 and listed in Table 1 (No. 1, 4). In order to compare the results with those in MB15, we use  $n_0 r_c^{3\beta}$  (instead of  $n_0$ ) as the normalization, even though we do not use a simplified power law to approximate Equation (1). As a result, we see a correlation in the best fit between the normalization and  $\beta$  in Figure 2. This is due to the degeneracy of the two parameters since  $\beta$  and  $n_0$  have opposite effects on the density at a fixed radius. The flatness (i.e.,  $\beta$ ) of the halo is crucial in determining

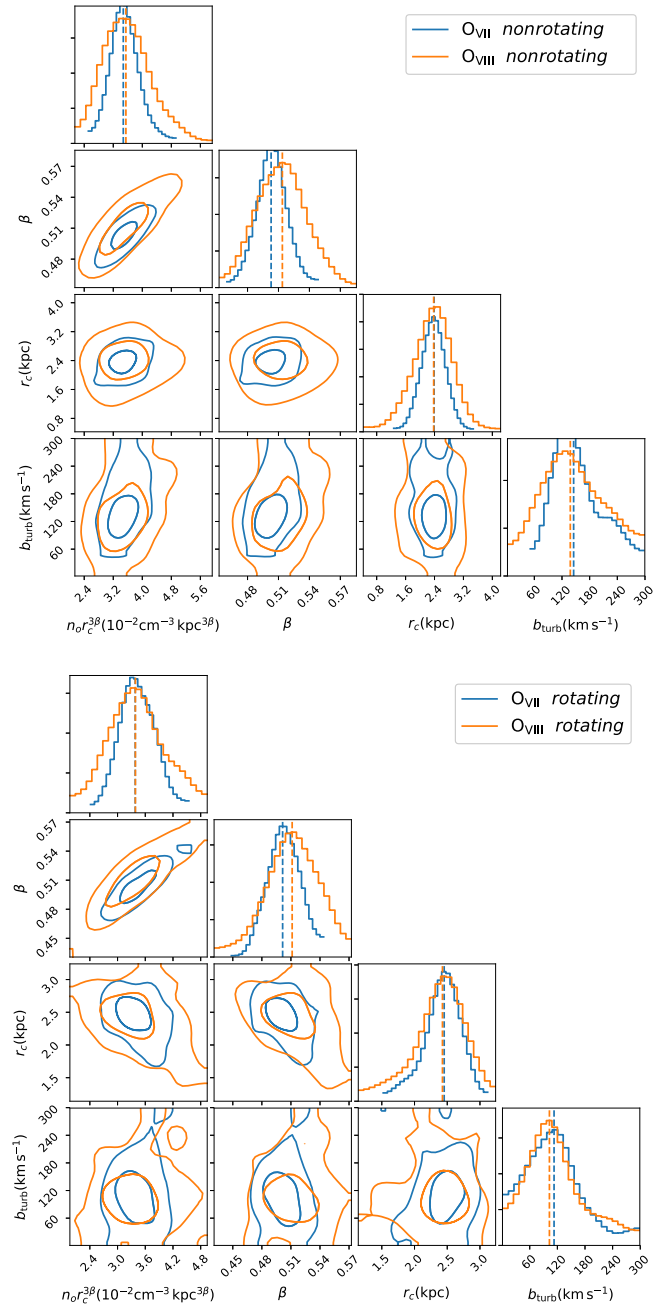


**Figure 2.** MCMC model parameters log-likelihood surface for O VII (blue) and O VIII (orange) in the stationary model (upper) and rotating model (lower) with  $v_\phi = 180 \text{ km s}^{-1}$ . The contours are for the  $1\sigma$  and  $2\sigma$  ranges, which correspond to a 39% and 86% confidence level in the 2D case.

the total baryon content of the halo. For the stationary case, we have  $\beta$  constrained at  $0.50 \pm 0.02$ , which is consistent with, if not slightly higher than, the results from emission line studies (Miller & Bregman 2015; Hodges-Kluck et al. 2016) and lower than those from absorption line studies assuming similar profiles (Miller & Bregman 2013; and model A of Nicastro et al. 2016). The core radius is also constrained at  $r_c = 2.4^{+0.3}_{-0.3}$  for O VII and  $r_c = 2.4^{+0.4}_{-0.5}$  for O VIII, which are consistent with the value  $2.1 \sim 2.5 \text{ kpc}$  found by Nicastro et al. (2016). This result comes as a surprise because the sight line in our data closest to the Galactic center has an angle of about  $30^\circ$ , while a core radius at  $\sim 2.4 \text{ kpc}$  corresponds to an angle of about  $16^\circ$ . The fourth plot in the left panel of Figure 2 shows the log-

**Table 1**  
Parameter Estimation Result

	No.	$V_\phi(r > 1 \text{ kpc})$ $\text{km s}^{-1}$	$n_0 r_c^{3\beta}$ $10^{-2} \text{ cm}^{-3} \text{ kpc}^{3\beta}$	$\beta$	$r_c$ $\text{kpc}$	$b_{\text{turb}}$ $\text{km s}^{-1}$	$\sigma_{\text{add}}$ L.U.	$n_{0,\text{disk}}$ $10^{-2} \text{ cm}^{-3}$	$z_h$ $\text{kpc}$	$\chi^2(\text{DoF})$	$M_{\text{halo}}(r \leq 250 \text{ kpc})$ $10^{10} M_\odot$	$M_{\text{disk}}(r \leq 50 \text{ kpc})^a$ $10^8 M_\odot$
O VIII	1	...	$3.55^{+0.65}_{-0.56}$	$0.51^{+0.02}_{-0.02}$	$2.38^{+0.40}_{-0.47}$	$138^{+90}_{-65}$	...	...	...	1.16(644)	$3.5^{+0.4}_{-0.6}$	...
	2	180	$3.39^{+0.67}_{-0.55}$	$0.51^{+0.03}_{-0.03}$	$2.43^{+0.30}_{-0.39}$	$103^{+78}_{-46}$	...	...	...	1.16(644)	$3.3^{+0.6}_{-0.7}$	...
	3	180	$2.86^{+0.62}_{-0.41}$	$0.51^{+0.03}_{-0.02}$	$2.44^{+0.48}_{-0.35}$	$92^{+62}_{-46}$	...	$3.62^{+2.73}_{-1.39}$	$0.97^{+1.46}_{-0.68}$	1.12(642)	$2.8^{+0.3}_{-0.8}$	$1.3^{+0.6}_{-0.7}$
O VII	4	...	$3.48^{+0.38}_{-0.31}$	$0.50^{+0.01}_{-0.01}$	$2.39^{+0.28}_{-0.31}$	$145^{+76}_{-39}$	...	...	...	5.06(644)	$3.9^{+0.2}_{-0.5}$	...
	5	...	$3.48^{+0.36}_{-0.42}$	$0.50^{+0.01}_{-0.02}$	$2.09^{+0.39}_{-0.55}$	$224^{+56}_{-65}$	2.1	...	...	1.77(644)	$3.9^{+0.5}_{-0.4}$	...
	6	180	$3.38^{+0.42}_{-0.29}$	$0.50^{+0.02}_{-0.01}$	$2.45^{+0.23}_{-0.28}$	$113^{+50}_{-62}$	...	...	...	4.97(644)	$3.8^{+0.4}_{-0.6}$	...
	7	180	$3.60^{+0.43}_{-0.33}$	$0.51^{+0.01}_{-0.01}$	$2.30^{+0.34}_{-0.42}$	$125^{+55}_{-64}$	2.1	...	...	1.74(644)	$3.5^{+0.5}_{-0.3}$	...
	8	180	$2.99^{+0.26}_{-0.32}$	$0.52^{+0.01}_{-0.01}$	$2.67^{+0.28}_{-0.20}$	$115^{+34}_{-24}$	...	$3.99^{+1.31}_{-0.83}$	$1.25^{+0.49}_{-0.44}$	4.54(642)	$2.5^{+0.5}_{-0.3}$	$1.8^{+0.3}_{-0.4}$
	9	180	$2.82^{+0.34}_{-0.29}$	$0.51^{+0.02}_{-0.01}$	$2.53^{+0.17}_{-0.18}$	$110^{+47}_{-43}$	2.1	$3.82^{+1.03}_{-0.74}$	$1.34^{+0.51}_{-0.43}$	1.56(642)	$2.8^{+0.5}_{-0.4}$	$1.8^{+0.2}_{-0.3}$

**Note.**

<sup>a</sup> The density is converted from the  $I_{0,\text{disk}}$  by assuming the same temperature and metallicity for the disk as that of the halo.



likelihood surface of the nonthermal part of the Doppler parameter,  $b_{\text{turb}}$ ; the O VII and O VIII results both indicate that the plasma is turbulent at a speed of about  $>140 \text{ km s}^{-1}$  (near the speed of sound at  $200 \text{ km s}^{-1}$ ). There is also a weak degeneracy between  $n_0 r_c^{3\beta}$  and  $b_{\text{turb}}$  in the model because the two parameters act oppositely in determining the optical depth (Equations (9) and (10)).

Even though the parameter estimations for the both ions are similar, there is a difference in the goodness of the fitting, which was also a problem in MB15. In the stationary model, we have four parameters to be explored (all shown in Figure 2), therefore the degree-of-freedom in the  $\chi^2$  fitting is 644. Hereafter, we use the reduced  $\chi_{644}^2$  ( $\chi^2$  per degree-of-freedom) as the indicator of the goodness-of-fit. For O VIII, the best fit gives a  $\chi_{644}^2 = 1.16$ , which is acceptable, whereas the  $\chi_{644}^2$  for O VII is as high as 5.06. MB15 decrease the  $\chi^2$  to an acceptable value by adding an additional variation,  $\sigma_{\text{add}} = 2.1 \text{ L.U.}$  to the O VII lines; a similar technique is also used in Miller & Bregman (2013) for their O VII absorption line study. The deviation can be caused by variations in the SWCX, in the density/temperature profile, in the LB emission, or in the optical depths. According to the analyses in their paper, the SWCX postulation can be ruled out since they did not find an emission excess near the ecliptic plane and there was little difference between the fitting using only the sight lines near the ecliptic plane and the sight lines in the opposite directions. The variations of the halo density/temperature profile and the LB emission are both plausible since the models are quite idealistic in either case. We do not attempt to distinguish these scenarios and use the additional 2.1 L.U. variation. The  $\sigma_{\text{add}}$  is added to the statistical and systematic uncertainties (from Henley & Shelton 2012) in quadrature.

#### 4.2. Corotating Model Parameter Estimation

The efficiency of the simulation drops by about an order of magnitude when rotation is introduced. Therefore we use fewer photons ( $10^4$ ) in each MCMC step. Nevertheless, the MCMC procedure still gives a reliable parameter estimation. The presence of the rotation affects the radiative transfer in the halo and in turn modifies the parameter estimation; we present the contours on the lower panel in Figure 2. The differences between the normalization and  $\beta$  remain, while the estimation for the core radius reaches better agreement at  $\approx 2.4 \text{ kpc}$ . The primary difference between the stationary case and the corotating case is the nonthermal Doppler  $b_{\text{turb}}$  estimation, which decreases to  $\approx 110 \text{ km s}^{-1}$  for both ions in the presence of rotation. As shown in Table 1, the estimations of the  $b_{\text{turb}}$  for corotating model (models 2, 6, and 7) are systematically lower than the estimation of the stationary model (models 1, 4, and 5). Combining this with the results from Figure 1, we see that this effect can be explained by the line-broadening effect of the halo rotation.

However, the rotation model is not necessarily a better description of the observation in terms of  $\chi_{644}^2$ , which is 4.97 and 1.16 for O VII and O VIII, respectively. We therefore also add the variation  $\sigma_{\text{add}} = 2.1 \text{ L.U.}$  to the O VII data, making sure that the parameter estimation is not biased by a few sight lines with small intrinsic uncertainties.

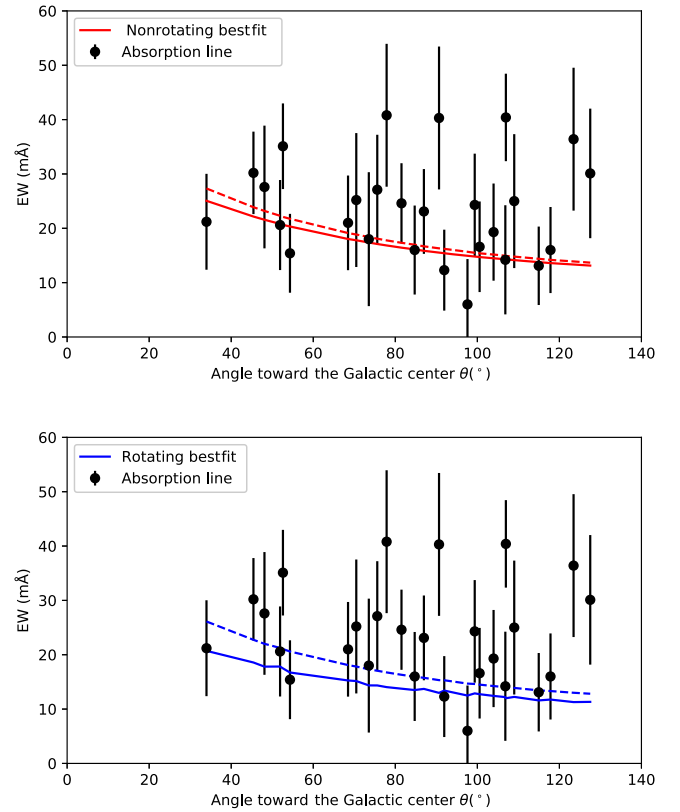


**Figure 3.** Comparison of the EW for the data and the model. The data are a subset of the data (27 of 37 sight lines) in Table 1 of Hodges-Kluck et al. (2016), with 10 sight lines with the highest uncertainties removed for illustration purposes. The EW measurement has very small uncertainties, therefore we likewise adopted an additional uncertainty of  $7.5 \text{ mÅ}$  in the EW of each sight line, as was introduced in Miller & Bregman (2013) to account for our lack of knowledge of the intrinsic variance due to the substructure of the absorbing medium. The red and blue solid lines show the EW toward the same sight lines for models 5 and 7 (also with additional uncertainties of  $2.1 \text{ L.U.}$ ), with the dashed lines being their  $2\sigma$  upper limit.

## 5. Discussion

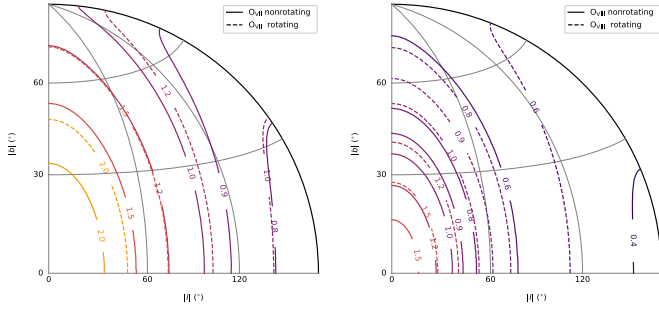
### 5.1. Consistency with the Absorption Line Data

The different mechanisms of emission and absorption along with their different dependencies on the density of the ions make the cross check between the observation on emission lines and absorption lines very important in revealing the structure of the hot gaseous halo (e.g., Gupta et al. 2012). We calculate the EW of our best-fit models in directions where the absorption line data are available (Hodges-Kluck et al. 2016) and present the result in Figure 3. It appears that the model built upon the emission line data underestimates the absorption line EW values by about 36% (as measured by the median value). However, this result is consistent with the EW measurement in the way that the EW data with higher values generally have larger uncertainties. Therefore we find it not very helpful in improving the  $\chi^2$  calculation with regard to the EW data by tuning the density normalization of the model (i.e., shifting the model curves upward to meet the majority of the EW data).

### 5.2. Optical Depth Effects

We are able to map the optical depth for the two types of lines across the sky with the best-fit parameters. The optical





### 5.3. Turbulence

We set constraints on the turbulence  $b_{\text{turb}}$  of the gaseous halo by carrying out radiative transfer simulation. For the stationary model fitting, we obtain systematically higher  $b_{\text{turb}}$  for both ion lines ( $\sim 150 \text{ km s}^{-1}$ ). However, when the galactic rotation is included in the model, we see that the values drop to  $90 \sim 120 \text{ km s}^{-1}$ . This can be explained by the line-broadening effect of the rotation, as mentioned in Section 2.4. The total Doppler  $b$  in the corotating case would be  $100 \sim 130 \text{ km s}^{-1}$ , which is consistent with the results in Gupta et al. (2012), Fang et al. (2015), and Nicastro et al. (2016). However, our result is a global model that includes the corotation of the halo, while the previous models are based on sight-line to sight-line observations. It is also interesting to point out that Nicastro et al. (2016) analyze the low galactic latitude and high galactic latitude absorption lines and find that the former have a larger average Doppler- $b$   $125 \text{ km s}^{-1}$  compared to the latter  $95 \text{ km s}^{-1}$ . This can be explained by our rotation-induced broadening effect (Miller & Bregman 2016; and Figure 1) and can be further examined by high spectral resolution line profile analyses or a longitudinal study.

If we regard the  $b_{\text{turb}}$  estimation obtained from the rotating-halo model as the true turbulence of the hot gaseous halo, we have  $b_{\text{turb}} \approx 100 \text{ km s}^{-1}$ . With the speed of sound of the halo  $c_s = 220 \text{ km s}^{-1}$ , we obtained the pressure contribution from the two components,

$$\frac{P_{\text{th}}}{P_{\text{turb}}} = \frac{\rho c_s^2 / \gamma}{\rho \sigma^2} = 1.2 \times \frac{c_s^2}{b_{\text{turb}}^2} \approx 5.8, \quad (12)$$

where  $\gamma = \frac{5}{3}$  is the adiabatic index. This value is lower than the result from the circumgalactic medium simulation (about 12; Fielding et al. 2017), but it is consistent with the general picture of massive galaxy formation (Birnboim & Dekel 2003), which posits that the halo can maintain hydrostatic equilibrium with the thermal support. This shows a particular level of feedback, which can be important to modelers.

### 5.4. Disk-like Component

The spherical-halo model is justified by the fitting, but some observations of absorption lines toward individual sources have been fit with a disk-like halo (Yao & Wang 2005; Yao et al. 2009; Hagihara et al. 2010) with a scale height of a few kpc or less (Nicastro et al. 2016). Additionally, observations of low-ionization lines are also successfully interpreted with an exponential disk model. This disk component is a natural consequence of supernova events in the MW disk. The outflow driven by the supernova feedback can maintain a disk-like halo at a temperature of  $\sim 10^6 \text{ K}$ , but the detailed shape, extent, and temperature of this halo strongly depend on the supernova history, the temperature of the mid-plane, and radiative cooling.

Hodges-Kluck et al. (2016) use the same MCMC method as MB15, but add an exponential disk in the fitting. Likewise, we add an exponential disk to both the stationary model and the corotating model, but we assume that the density of the disk decreases exponentially both along the  $z$  direction and the  $r$  direction since we should not expect that the disk can be sustained at larger radii where the MW disk fades out. The profile is

$$n_{\text{disk}} = n_{o,\text{disk}} e^{-r/r_h} e^{-z/z_h}. \quad (13)$$

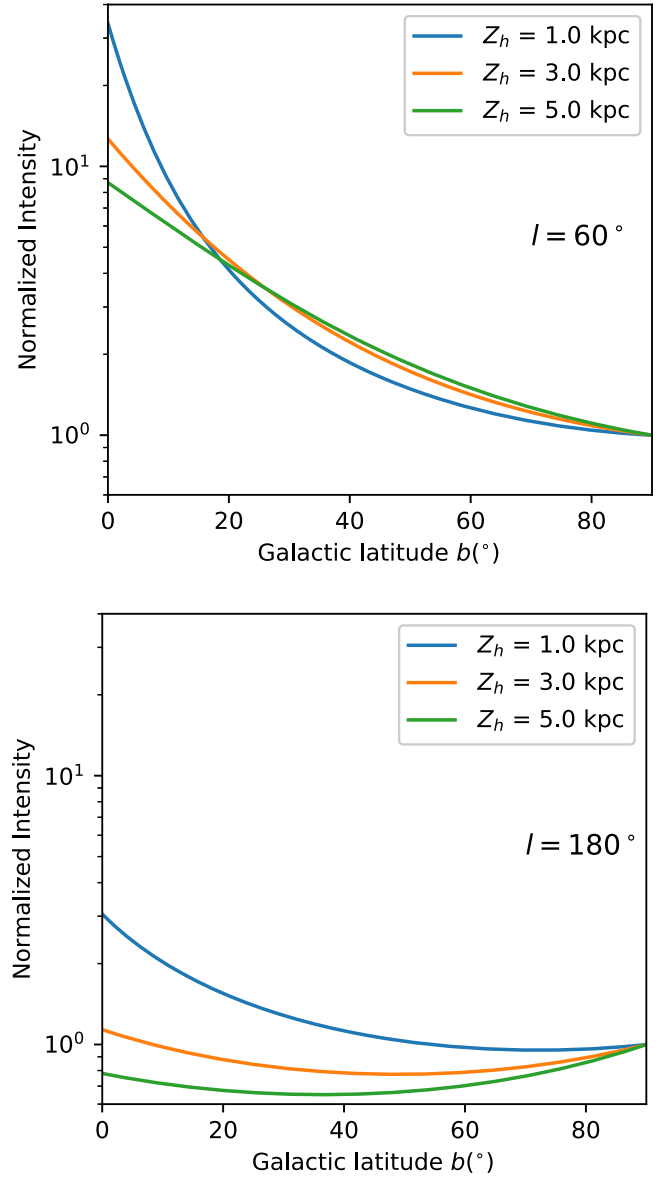


**Figure 7.** Comparison between disk emission intensities at Galactic longitude  $l = 60^\circ$  and  $l = 180^\circ$  as a function of Galactic latitude for different  $z_h$ . The curves are normalized at  $b = 90^\circ$  to illustrate the differences in latitudinal dependence.

This radial dependency of the disk density leads to distinct differences from the former disk model at certain directions. While the intensities toward  $l = 60^\circ$  decrease with Galactic latitudes, as we would expect from a normal disk model, the emission intensities can rise at high Galactic latitudes at  $l = 180^\circ$  for thick disks (Figure 7). This makes the direction toward  $l = 180^\circ$  a useful probe for different disk models.

We first make a test with a pure disk model and find that it cannot be fit with O VIII data. For O VII lines the  $\chi^2_{646} = 6.05$  is no better than the spherical-halo models. Therefore, the disk component, if exists, should come as a complement of the spherical halo. For simplicity, we assume that the disk and the halo share the same metallicity and temperature. We fix the scale radius at  $r_h = 3 \text{ kpc}$  and leave  $z_h$  to be a free parameter. The fitting is made only for the corotating model because of its cylindrical symmetry. The results are listed in Table 1 (models 3, 8, and 9).

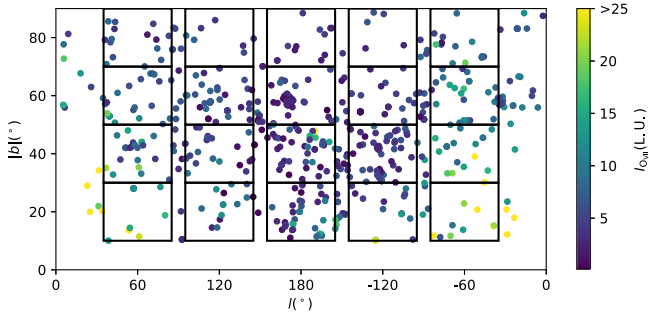


**Figure 8.** Emission map of O VII and the bins used for statistics. The equal-size bins are chosen to cover most of the sight lines. The emission measure of each bin is assigned as the weighted mean of the intensity of the sight lines inside the bin. The weight is defined as the inverse of the uncertainty.

We bin the sight lines in the way illustrated in Figure 8, and show in Figure 9 the emission measure of the O VII data at different longitudes and latitudes. The spherical-halo model (red) underestimates the emission at lower latitudes, while a spherical halo with a disk component (blue) makes a better fit. In particular, the spherical-halo model and the disk model can be distinguished by their performance along the latitudes at  $l = 180^\circ$  (the last panel in Figure 9) since we would expect from the spherical halo a higher emission measure at higher latitudes toward which the path length is greater, while the disk model ( $z_h \sim 1$  kpc) makes an opposite prediction. The O VII data in the last panel shows a decreasing pattern with increasing latitude, and the spherical-halo + disk model reduces the differences between the single-halo model and the data (by a factor  $\lesssim 2$  at lower  $b$ ). The fitting is made globally, and the improvement in one single panel is limited. The averaging shown in Figure 9 enables one to better comprehend how different components influence the fit.

The results of the fitting (Table 1) show that observation and model are brought closer in the presence of an exponential disk, and the scale height of the disk inferred from O VII lines is constrained within the range  $\sim 1.3$  kpc, while that from O VIII is less constrained. This disk is thinner than the results in Yao et al. (2009) and Hagihara et al. (2010) because the disk in our model only contributes to a small portion of the emission. Our disk is thicker than the 0.16 kpc disk from the low Galactic latitude line analyses in Nicastro et al. (2016), but the results are consistent in the sense that both disks contribute to a similar small portion of baryon mass  $1.4 \times 10^8 M_\odot$  (Table 1). It is worth pointing out that the spherical halo plus disk model in Nicastro et al. (2016) finds a smaller  $\beta = 0.33$  than  $\beta = 0.62$  in the spherical  $\beta$ -model, while the extra disk component in our model improves the fit at lower Galactic latitudes without significantly affecting the  $\beta$ -model parameters. Therefore, although the disk masses are low in both models, they result in different total masses.

The baryon mass contribution from the disk is two orders of magnitude lower than that of the halo, which leads us to the conclusion that the disk only makes up a small portion of the ion column, and this is also consistent with the previous z-exponential model ( $\approx 10\%$ ; Hodges-Kluck et al. 2016). This halo part of the result is also consistent with that of the halo + disk fitting for same emission line data (Hodges-Kluck et al. 2016), although we update their disk model and their scale height, which was not well constrained.

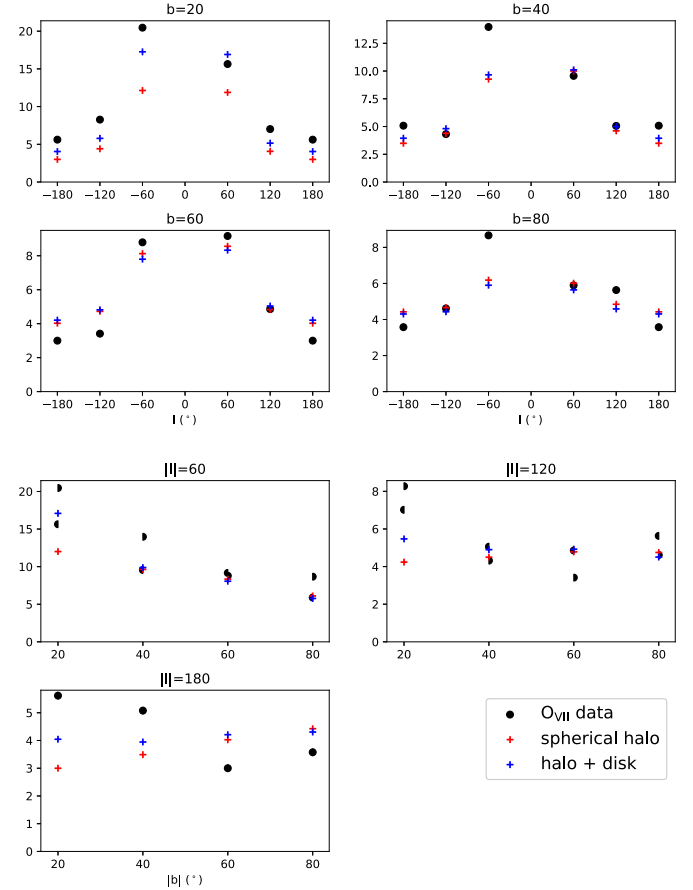


**Figure 9.** O VII emission intensities from the observations (black circles) and simulated emission map along the Galactic longitude ( $l$ ) at different Galactic latitudes ( $b$ ) (first four panels), and the emission along the Galactic latitude at different Galactic longitudes (last three panels). In the last three panels, the intensities of the data toward positive and negative longitudes are denoted with left-filled and right-filled circles. The alignments of the bins are shown in Figure 8. We simulated the emission map of two models: the spherical halo with rotation is plotted in red, and the spherical halo with rotation and a disk is shown in blue. The parameters of these two models are acquired through fittings 7 and 9. The spherical halo with a disk fits the observation better in the way that it increases the emission measure at lower latitudes, while the spherical-halo model is unable to reproduce the latitudinal variation.

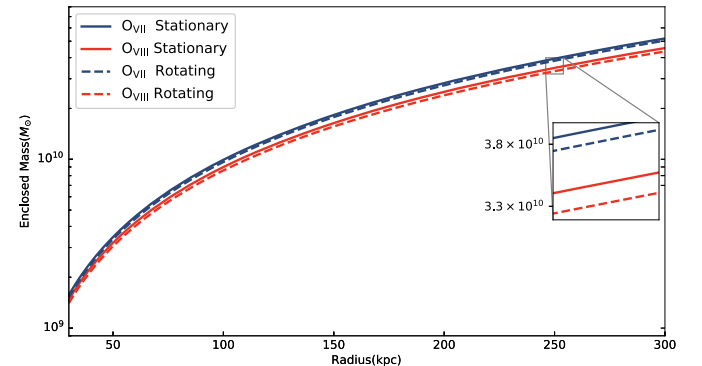


**Figure 10.** Enclosed baryon mass of the halo vs. radii inferred from the best fit of different models. The metallicity used is  $0.3Z_\odot$ . The uncertainties can be found in Table 1.

### 5.5. Baryon Budget

With the better constraint of the halo parameters, we update the baryon mass estimation of the Milky Way halo (Figure 10). We find that the gas mass estimations are not sensitive to the

uncertainties in the parameters. At the virial radius of 250 kpc, the enclosed mass is about  $3.1^{+0.5}_{-0.3} \times 10^{10} M_{\odot}$  and can only account for 18% of the missing baryon mass ( $1.7 \times 10^{11} M_{\odot}$ , after the exclusion of the contribution from the stars and cold gas.). The data from the Galactic center and the FB are not used in modeling, and the density profile we obtain here might not properly describe these structures. Nevertheless, it is shown that the central region of the Galaxy is either depleted of gas (Kataoka et al. 2015; Nicastro et al. 2016) or contains a fractional mass compared to the halo mass ( $10^{7-8} M_{\odot}$ , Miller & Bregman 2016; Nicastro et al. 2016).

Further improvements in interpreting the emission can be achieved with higher spectral resolution data, which would permit one to isolate lines and obtain a better S/N for each line. Such an improved resolution is likely to become available from future missions with calorimeters, which have a sufficiently high resolution to split the O VII triplet, of which two of the lines have low optical depth. Measuring each of the O VII triplet lines has the potential of separating cooler and hotter gas, as well as of more accurately separating the contribution from solar wind charge exchange and the LB. Higher spectral resolution observations will allow one to determine line center shifts, which further constrain halo rotation and turbulent broadening. Higher S/N data will allow for better measures of the O VIII Ly $\alpha$  line as well as recombination from higher level recombination lines, which have lower optical depths. Together, these will lead to a more detailed and precise description of the Milky Way hot halo. A calorimeter would be one of the main instruments on a replacement mission for Hitomi (Takahashi et al. 2016), the Athena mission (Barret 2016), or the Lynx mission (Gaskin et al. 2015).

We thank everyone who offered their help to this work, including Matthew Miller, Edmund Hodges-Kluck, Zhijie Qu, and our anonymous referee, whose comments helped to improve this work. Special thanks also go to Eric Peng for the computational resources he provided. This research is funded by the China Scholarship Council, NASA ADAP grant NNX16AF23G, and the Department of Astronomy at the University of Michigan, who we also thank for their hospitality.

*Software:* AtomDB (Foster et al. 2012), emcee (Foreman-Mackey et al. 2013).

## ORCID iDs

Yunyang Li  <https://orcid.org/0000-0002-4820-1122>

## References

- Anders, E., & Grevesse, N. 1989, *GeCoA*, **53**, 197
- Anderson, M. E., & Bregman, J. N. 2011, *ApJ*, **737**, 22
- Anderson, M. E., Churazov, E., & Bregman, J. N. 2016, *MNRAS*, **455**, 227
- Balucinska-Church, M., & McCammon, D. 1992, *ApJ*, **400**, 699
- Barret, D., Lam Trong, T., den Herder, J.-W., et al. 2016, *Proc. SPIE*, **9905**, 99052F
- Birboim, Y., & Dekel, A. 2003, *MNRAS*, **345**, 349
- Bogdán, Á., Forman, W. R., Kraft, R. P., & Jones, C. 2013a, *ApJ*, **772**, 98
- Bogdán, Á., Forman, W. R., Vogelsberger, M., et al. 2013b, *ApJ*, **772**, 97
- Bregman, J. N. 2007, *ARA&A*, **45**, 221
- Bregman, J. N., & Houck, J. C. 1997, *ApJ*, **485**, 159
- Bregman, J. N., & Lloyd-Davies, E. J. 2007, *ApJ*, **669**, 990
- Cen, R., & Ostriker, J. P. 2006, *ApJ*, **650**, 560
- Cox, D. P., & Reynolds, R. J. 1987, *ARA&A*, **25**, 303
- Crain, R. A., McCarthy, I. G., Frenk, C. S., Theuns, T., & Schaye, J. 2010, *MNRAS*, **407**, 1403
- Dai, X., Anderson, M. E., Bregman, J. N., & Miller, J. M. 2012, *ApJ*, **755**, 107
- De Lucia, G., Springel, V., White, S. D. M., Croton, D., & Kauffmann, G. 2006, *MNRAS*, **366**, 499
- Dickey, J. M., & Lockman, F. J. 1990, *ARA&A*, **28**, 215
- Fang, T., Buote, D., Bullock, J., & Ma, R. 2015, *ApJS*, **217**, 21
- Fang, T., & Jiang, X. 2014, *ApJL*, **785**, L24
- Fang, T., McKee, C. F., Canizares, C. R., & Wolfire, M. 2006, *ApJ*, **644**, 174
- Fielding, D., Quataert, E., McCourt, M., & Thompson, T. A. 2017, *MNRAS*, **466**, 3810
- Flury, B. D. 1990, *SIAMR*, **32**, 474
- Foreman-Mackey, D., Hogg, D. W., Lang, D., & Goodman, J. 2013, *PASP*, **125**, 306
- Forman, W., Jones, C., & Tucker, W. 1985, *ApJ*, **293**, 102
- Foster, A. R., Ji, L., Smith, R. K., & Brickhouse, N. S. 2012, *ApJ*, **756**, 128
- Fox, A. J., Wakker, B. P., Savage, B. D., et al. 2005, *ApJ*, **630**, 332
- Fukugita, M., Hogan, C. J., & Peebles, P. J. E. 1998, *ApJ*, **503**, 518
- Fukugita, M., & Peebles, P. J. E. 2006, *ApJ*, **639**, 590
- Gaskin, J. A., Weisskopf, M. C., Vikhlinin, A., et al. 2015, *Proc. SPIE*, **9601**, 96010J
- Ghez, A. M., Salim, S., Weinberg, N. N., et al. 2008, *ApJ*, **689**, 1044
- Gibson, B. K., Giroux, M. L., Penton, S. V., et al. 2000, *AJ*, **120**, 1830
- Gupta, A., Mathur, S., Krongold, Y., Nicastro, F., & Galeazzi, M. 2012, *ApJL*, **756**, L8
- Hagihara, T., Yao, Y., Yamasaki, N. Y., et al. 2010, *PASJ*, **62**, 723
- Henley, D. B., & Shelton, R. L. 2010, *ApJS*, **187**, 388
- Henley, D. B., & Shelton, R. L. 2012, *ApJS*, **202**, 14
- Henley, D. B., & Shelton, R. L. 2013, *ApJ*, **773**, 92
- Hinshaw, G., Larson, D., Komatsu, E., et al. 2013, *ApJS*, **208**, 19
- Hodges-Kluck, E. J., Miller, M. J., & Bregman, J. N. 2016, *ApJ*, **822**, 21
- Holweber, H. 2001, in AIP Conf. Ser. 598, Joint SOHO/ACE Workshop “Solar and Galactic Composition”, ed. R. F. Wimmer-Schweingruber (Melville, NY: AIP), 23
- Joung, M. R., Putman, M. E., Bryan, G. L., Fernández, X., & Peek, J. E. G. 2012, *ApJ*, **759**, 137
- Kalberla, P. M. W., Burton, W. B., Hartmann, D., et al. 2005, *A&A*, **440**, 775
- Kataoka, J., Tahara, M., Totani, T., et al. 2015, *ApJ*, **807**, 77
- Kereš, D., Katz, N., Weinberg, D. H., & Davé, R. 2005, *MNRAS*, **363**, 2
- Kim, J.-h., Wise, J. H., & Abel, T. 2009, *ApJL*, **694**, L123
- Lallement, R. 2004, *A&A*, **418**, 143
- Lallement, R., Welsh, B. Y., Vergely, J. L., Crifo, F., & Sfeir, D. 2003, *A&A*, **411**, 447
- Li, J.-T., Li, Z., Wang, Q. D., Irwin, J. A., & Rossa, J. 2008, *MNRAS*, **390**, 59
- McCammon, D., Almy, R., Apodaca, E., et al. 2002, *ApJ*, **576**, 188
- McKernan, B., Yaqoob, T., & Reynolds, C. S. 2004, *ApJ*, **617**, 232
- Miller, M. J., & Bregman, J. N. 2013, *ApJ*, **770**, 118
- Miller, M. J., & Bregman, J. N. 2015, *ApJ*, **800**, 14
- Miller, M. J., & Bregman, J. N. 2016, *ApJ*, **829**, 9
- Miller, M. J., Hodges-Kluck, E. J., & Bregman, J. N. 2016, *ApJ*, **818**, 112
- Mo, H., van den Bosch, F. C., & White, S. 2010, *Galaxy Formation and Evolution* (Cambridge: Cambridge Univ. Press)
- Mulchaey, J. S., & Jeltima, T. E. 2010, *ApJL*, **715**, L1
- Nevalainen, J., Wakker, B., Kaastra, J., et al. 2017, *A&A*, **605**, A47
- Nicastro, F., Mathur, S., Elvis, M., et al. 2005, *Natur*, **433**, 495
- Nicastro, F., Senatore, F., Krongold, Y., Mathur, S., & Elvis, M. 2016, *ApJL*, **828**, L12
- Nicastro, F., Zezas, A., Drake, J., et al. 2002, *ApJ*, **573**, 157
- O’Sullivan, E., Forbes, D. A., & Ponman, T. J. 2001, *MNRAS*, **328**, 461
- Rasmussen, J., Sommer-Larsen, J., Pedersen, K., et al. 2009, *ApJ*, **697**, 79
- Robertson, I. P., & Cravens, T. E. 2003, *JGRA*, **108**, 8031
- Smith, R. K., Bautz, M. W., Edgar, R. J., et al. 2007, *PASJ*, **59**, 141
- Smith, R. K., Brickhouse, N. S., Liedahl, D. A., & Raymond, J. C. 2001, *ApJL*, **556**, L91
- Snowden, S. L., Cox, D. P., McCammon, D., & Sanders, W. T. 1990, *ApJ*, **354**, 211
- Snowden, S. L., Egger, R., Freyberg, M. J., et al. 1997, *ApJ*, **485**, 125
- Snowden, S. L., Freyberg, M. J., Plucinsky, P. P., et al. 1995, *ApJ*, **454**, 643
- Sommer-Larsen, J. 2006, *ApJL*, **644**, L1
- Su, M., Slatyer, T. R., & Finkbeiner, D. P. 2010, *ApJ*, **724**, 1044
- Sutherland, R. S., & Dopita, M. A. 1993, *ApJS*, **88**, 253
- Takahashi, T., Kokubun, M., Mitsuda, K., et al. 2016, *Proc. SPIE*, **9905**, 99050U



- Tang, S., Wang, Q. D., Lu, Y., & Mo, H. J. 2009, [MNRAS](#), **392**, 77
- Toft, S., Rasmussen, J., Sommer-Larsen, J., & Pedersen, K. 2002, [MNRAS](#), **335**, 799
- Tüllmann, R., Pietsch, W., Rossa, J., Breitschwerdt, D., & Dettmar, R.-J. 2006, [A&A](#), **448**, 43
- van Woerden, H., & Wakker, B. P. 2004, in *High Velocity Clouds*, ed. H. van Woerden, [195](#)
- Walker, S. A., Bagchi, J., & Fabian, A. C. 2015, [MNRAS](#), **449**, 3527
- Welsh, B. Y., & Shelton, R. L. 2009, [Ap&SS](#), **323**, 1
- White, S. D. M., & Frenk, C. S. 1991, [ApJ](#), **379**, 52
- Whitney, B. A. 2011, *BASI*, **39**, 101
- Williams, R. J., Mathur, S., Nicastro, F., et al. 2005, [ApJ](#), **631**, 856
- Williams, R. J., Mathur, S., & Nicastro, F. 2006, [ApJ](#), **645**, 179
- Williams, R. J., Mathur, S., Nicastro, F., & Elvis, M. 2007, [ApJ](#), **665**, 247
- Yan, M., Sadeghpour, H. R., & Dalgarno, A. 1998, [ApJ](#), **496**, 1044
- Yao, Y., Shull, J. M., Wang, Q. D., & Cash, W. 2012, [ApJ](#), **746**, 166
- Yao, Y., & Wang, Q. D. 2005, [ApJ](#), **624**, 751
- Yao, Y., Wang, Q. D., Hagihara, T., et al. 2009, [ApJ](#), **690**, 143